

APPENDIX

A. DERIVING DIAGNOSTIC LINE RATIOS FROM WFC3 FILTER IMAGES

The WFC3 camera is equipped with filters that effectively target important nebular diagnostic lines. Each filter, with label j , is characterized by an effective transmission profile, or throughput, T_λ^j , which gives the wavelength-dependent conversion factor between the number of photons arriving at the *HST* entrance aperture (nominal radius: 120 cm) and the number of electrons registered by the CCD, accounting for occultation by the secondary mirror, all other optical and quantum efficiencies, and the amplifier gain. The peak value of the filter transmission profile is denoted T_m^j , with typical values of 0.2–0.3, and the “rectangular width” of the profile is defined as

$$W_j = (T_m^j)^{-1} \int_0^\infty T_\lambda^j d\lambda \quad [W_j] = \text{\AA}. \quad (\text{A1})$$

Extensive and continuing on-orbit calibration of the filters has been carried out (Kalirai et al. 2009, 2010; Sabbi & the WFC3 Team 2013) using white dwarf standard stars. However, since these are flat featureless continuum sources, the calibration is only sensitive to the integrated filter throughput, given by the product $W_j T_m^j$. A general increase in the integrated throughput of 10–20% with respect to pre-launch measurements was found for all filters, which was fitted by a low-order polynomial as a function of frequency. Only the broad-band and medium-band filters were used in determining the fit, but the scatter of the narrow-band filters¹ around the resulting curve is only a few percent (see Fig. 6 of Kalirai et al. 2009).

Emission lines from photoionized regions are intrinsically much narrower than even the narrowest WFC3 filters, so the transmission of such a line, with label i , is independent of W_j and depends instead solely on the throughput at the line wavelength: $T_i^j \equiv T_\lambda^j(\lambda = \lambda_i)$. The detailed shape of the throughput curves was measured pre-launch (Brown 2006), but direct on-orbit confirmation of these curves is impossible. However, by comparing WFC3 images with ground-based spectrophotometry of emission line nebulae, it is possible to test the filter calibrations for the case where emission lines are the dominant component of the spectrum in the filter bandpass.

We model the specific intensity, I_λ (in $\text{erg s}^{-1} \text{cm}^{-2} \text{sr}^{-1} \text{\AA}^{-1}$), of a spatially resolved astrophysical source as the sum of several narrow emission lines i , each with central wavelength λ_i and wavelength-integrated intensity I_i , plus a slowly varying continuum I_λ^c :

$$I_\lambda = I_\lambda^c + \sum_{i=1,n} I_i \delta(\lambda - \lambda_i), \quad (\text{A2})$$

where δ denotes the Dirac delta function. It is convenient to define an average continuum intensity over the passband of filter j :

$$\langle \lambda I_\lambda^c \rangle_j = \int_0^\infty \lambda I_\lambda^c T_\lambda^j d\lambda / \int_0^\infty T_\lambda^j d\lambda. \quad (\text{A3})$$

The count rate (in e^-/s) in a single pixel of a pipeline-reduced (bias-subtracted, flat-fielded, drizzled) WFC3 image should then be

$$R_j = C_{\text{WFC3}} \left(\langle \lambda I_\lambda^c \rangle_j T_m^j W_j + \sum_{i=1,n} \lambda_i I_i T_i^j \right) \quad (\text{A4})$$

where $C_{\text{WFC3}} = 10^{-8} A_{\text{HST}} \Omega_{\text{pix}} / (hc) = 0.0840241 \text{ counts cm}^2 \text{sr erg}^{-1} \text{\AA}^{-1} \text{pixel}^{-1}$ is a constant for the camera, depending on the telescope aperture area, $A_{\text{HST}} = \pi(120 \text{ cm})^2 = 45,239 \text{ cm}^2$, and the solid-angle subtended² by each pixel $\Omega_{\text{pix}} = (0.03962'')^2 = 3.6895 \times 10^{-14} \text{ sr}$.

We now consider the particular application of deriving a diagnostic ratio between two emission lines: I_1/I_2 . It is assumed that observations are made in three filters: Filter I, which targets line 1, Filter II, which targets line 2, and Filter III, which targets the continuum. For optimum results, filters I and II will be narrow-band in order to admit as little continuum as possible, while III will be medium-band so as to efficiently sample the continuum, while at the same time avoiding strong emission lines. However, in practice it is usually impossible to completely avoid emission line contamination of filter III, either by one or both of the target lines (1 and 2), or by other lines that we denote i' . A schematic illustration of this situation is given in Figure 10. For given line

¹ Note, however, that the quad filters were not included in these studies.

² Although geometric distortions by the telescope optics mean that the true pixel area varies across the field of view, this is corrected for during the “drizzle” stage of the pipeline reduction process, which yields images (extension drz) interpolated onto a regular pixel grid. If non-drizzled (extension f1t) images are used, then a further correction for the pixel area map must be applied to equation (A4).

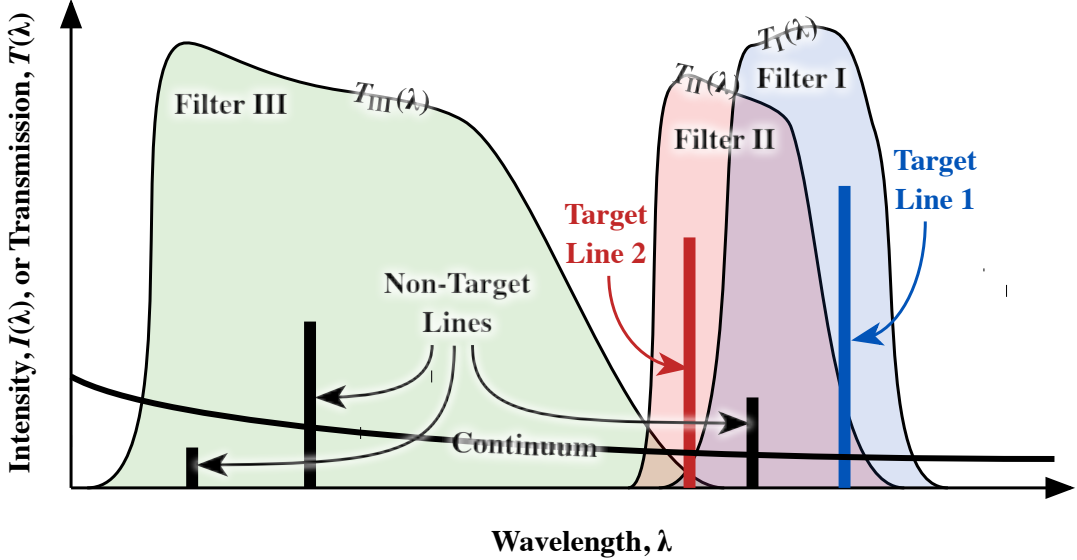


FIG. 10.— Schematic illustration of how the intensity ratio between two target lines is derived using observations in three filters.

and continuum intensities, I_1 , I_2 , I_λ^c , the predicted filter rates are:

$$R_I = C_{\text{WFC3}} \left[\langle \lambda I_\lambda^c \rangle_I T_m^I W_I + \lambda_1 I_1 T_1^I + \lambda_2 I_2 T_2^I + \sum_{i' \neq 1,2} \lambda_{i'} I_{i'} T_{i'}^I \right] \quad (\text{A5})$$

$$R_{II} = C_{\text{WFC3}} \left[\langle \lambda I_\lambda^c \rangle_{II} T_m^{II} W_{II} + \lambda_1 I_1 T_1^{II} + \lambda_2 I_2 T_2^{II} + \sum_{i' \neq 1,2} \lambda_{i'} I_{i'} T_{i'}^{II} \right] \quad (\text{A6})$$

$$R_{III} = C_{\text{WFC3}} \left[\langle \lambda I_\lambda^c \rangle_{III} T_m^{III} W_{III} + \lambda_1 I_1 T_1^{III} + \lambda_2 I_2 T_2^{III} + \sum_{i' \neq 1,2} \lambda_{i'} I_{i'} T_{i'}^{III} \right] \quad (\text{A7})$$

The mean continuum intensity in the narrow filters can be related to that in the wider filter by defining color terms:

$$k_{j,III} \equiv \frac{\langle \lambda I_\lambda^c \rangle_j}{\langle \lambda I_\lambda^c \rangle_{III}} \quad \text{for } j = I, II \quad (\text{A8})$$

The filter color terms can be formally extended to include the contribution of contaminating non-target emission lines:

$$\tilde{k}_{j,III} \equiv \frac{\langle \lambda I_\lambda^c \rangle_j + (T_m^j W_j)^{-1} \sum_{i' \neq 1,2} \lambda_{i'} I_{i'} T_{i'}^j}{\langle \lambda I_\lambda^c \rangle_{III} + (T_m^{III} W_{III})^{-1} \sum_{i' \neq 1,2} \lambda_{i'} I_{i'} T_{i'}^{III}} = \frac{(1 + \sum_{i' \neq 1,2} E_{i'}/\tilde{W}_{j,i'}) k_{j,III}}{1 + \sum_{i' \neq 1,2} E_{i'}/\tilde{W}_{III,i'}} \quad (\text{A9})$$

where the $E_{i'}$ are the equivalent width (in Å) of each non-target line and we have also introduced an “effective width” of each filter with respect to a given emission line:

$$\tilde{W}_{j,i} \equiv k_{j,i} \frac{T_m^j}{T_i^j} W_j \quad \text{with} \quad k_{j,i} \equiv \frac{\langle \lambda I_\lambda^c \rangle_j}{\lambda_i I_\lambda^i}. \quad (\text{A10})$$

Note that the effective width has the property that $\tilde{W}_{j,i} \approx W_j$ for lines i that lie comfortably within the bandpass of filter j , whereas $\tilde{W}_{j,i} > W_j$ for lines that lie on the edge of the bandpass, where the filter transmission is reduced, and $\tilde{W}_{j,i} \rightarrow \infty$ for lines far-removed from the filter bandpass.

With these definitions, equations (A5) to (A7) can be recognised as being equivalent to a single matrix equation that gives the vector of count rates, $[R_I ; R_{II} ; R_{III}]$, in terms of the vector of intensities, $[\lambda_1 I_1 ; \lambda_2 I_2 ; \langle \lambda I_\lambda^c \rangle_{III}]$. Therefore, in order to solve for the intensities in terms of the count rates it is sufficient to invert the matrix. The result for the line ratio is then:

$$\frac{I_1}{I_2} = \frac{\lambda_2 T_2^{II} \left[(1 - \alpha_2 \beta_{II} \tilde{k}_{II,III}) R_I + (\alpha_2 \beta_I \tilde{k}_{I,III} - \gamma_2) R_{II} + (\gamma_2 \beta_{II} \tilde{k}_{II,III} - \beta_I \tilde{k}_{I,III}) R_{III} \right]}{\lambda_1 T_1^I \left[(\alpha_1 \beta_I \tilde{k}_{I,III} - \gamma_1) R_I + (1 - \alpha_1 \beta_I \tilde{k}_{I,III}) R_{II} + (\gamma_1 \beta_I \tilde{k}_{I,III} - \beta_{II} \tilde{k}_{II,III}) R_{III} \right]} \quad (\text{A11})$$

TABLE 1
FILTER CONTAMINATION COEFFICIENTS, SEE Eqs. (A11, A12)

Ratio: I_1/I_2	Filter Set: I, II, III	α_1	α_2	β_1	β_{II}	γ_1	γ_2
[N II] 5755/6583	FQ575N, F658N, F547M	0.7946	~ 0	0.0243	0.0394	~ 0	~ 0
[S II] 6716/6731	FQ672N, FQ674N, F673N	1.0580	1.2510	0.1640	0.1142	0.0702	0.0056
[S II] 6716/6731	FQ672N, FQ674N, F547M	~ 0	~ 0	0.0274	0.0191	0.0702	0.0050
[O III] 4363/5007	FQ437N, F502N, FQ436N	0.9170	~ 0	0.711	1.998	~ 0	~ 0
[O III] 4363/5007	FQ437N, F502N, F547M	~ 0	0.0016	0.0343	0.0963	~ 0	~ 0
H β /H α 4861/6563	F487N, F656N, F547M	~ 0	~ 0	0.0871	0.0238	~ 0	~ 0
[N II]/H α 6583/6563	F658N, F656N, F547M	~ 0	~ 0	0.0394	0.0238	~ 0	0.0022
[O III]/H β 5007/4861	F502N, F487N, F547M	0.0016	~ 0	0.0963	0.0871	~ 0	~ 0

NOTE: Values marked as “~ 0” are all less than 10^{-5} .

with filter contamination coefficients

$$\alpha_1 = \frac{T_1^{\text{III}}}{T_1^{\text{I}}}; \quad \alpha_2 = \frac{T_2^{\text{III}}}{T_2^{\text{II}}}; \quad \beta_1 = \frac{T_m^{\text{I}} W_1}{T_m^{\text{III}} W_{\text{III}}}; \quad \beta_{\text{II}} = \frac{T_m^{\text{II}} W_{\text{II}}}{T_m^{\text{III}} W_{\text{III}}}; \quad \gamma_1 = \frac{T_1^{\text{II}}}{T_1^{\text{I}}}; \quad \gamma_2 = \frac{T_2^{\text{I}}}{T_2^{\text{II}}}.$$
 (A12)

The α contamination coefficients give the throughput of each target emission line in the continuum filter III relative to the throughput in its respective narrow-band filter, and will tend to be either ~ 1 for lines that fall in the continuum bandpass, or ~ 0 for those that do not. The β contamination coefficients give the integrated continuum throughput in each narrow band filter relative to the continuum filter. The γ contamination coefficients give the throughput of each target emission line in the “other” narrow band filter relative to the throughput in its own narrow-band filter, and will only be important in cases where the two narrow band filters overlap.

Since repeated calibration programs have shown that the WFC3 filter characteristics are stable with time, all these purely instrumental coefficients are constants, albeit with a small systematic uncertainty in their true value. The k factors, on the other hand, represent the relative strengths of the continuum and non-target lines in the bandpasses of the three filters, and are expected to show variations from object to object and from pixel to pixel within the same object, due to changes in the physical conditions.

B. CALIBRATION OF WFC3 FILTERS USING THE MUSE SPECTROSCOPIC DATASET

In this appendix we make use of the VLT-MUSE integral field spectroscopic dataset of the Orion Nebula (Weilbacher et al. 2015) to test and calibrate the filter-based technique for deriving line ratios outlined in the previous section. There are two independent checks that need to be made: (1) photometric calibration of all the relevant WFC3 filters, and (2) verification that equation (A11) can accurately recover emission line ratios, even in the face of uncontrolled for variations in the continuum color. These are each considered in turn.

B.1. Photometric comparison of WFC3 filter images with synthetic images derived from MUSE spectral cube

In order to compare the photometry of the two instruments, it is necessary to transform both datasets to a common scale. The processing steps for the MUSE datacube are as follows:

M1. For each WFC3 filter bandpass a sub-cube is extracted containing only the spectral window containing the filter. The window is centered on the filter average wavelength and with a width equal to twice the rectangular width of the filter. Separate files are extracted for the data and variance cubes. Due to the large size (110 GB) of the full datacube, this step is carried out on a powerful server. The windowed sub-cubes have much smaller file sizes, ranging from 0.5 to 15 GB depending on the filter width, allowing subsequent steps to be comfortably carried out on a laptop computer.

M2. Each 3-dimensional sub-cube is folded through the filter bandpass profile T_λ^j to derive a 2-dimensional synthetic simulated filter image:

$$R_j = C_{\text{WFC3}} \int \lambda I_\lambda T_\lambda^j d\lambda,$$
 (B1)

where R_j is the predicted count rate (electron per second per WFC3 pixel) in the j th filter and I_λ is the wavelength-dependent surface brightness in $\text{erg s}^{-1} \text{cm}^{-2} \text{sr}^{-1} \text{\AA}^{-1}$. The constant C_{WFC3} is discussed following equation (A4) above. In order to convert the MUSE data values to the correct units for I_λ it is necessary to multiply by 10^{-20} and divide by the MUSE pixel area of $9.40175 \times 10^{-13} \text{ sr}$. The bandpasses T_λ are obtained from the `pysynphot` Python library³, which uses reference files from the Calibration Reference Database System (CRDS, replacing the older CDBS)⁴ of STScI. In this step it is important to translate the filter wavelengths from the vacuum scale that is used in the reference files to the air scale used in the MUSE cube.

M3. Finally, the resulting image is cropped to the same field of view as the WFC3 image.

The processing steps for the HST WFC3 images are as follows:

W1. The angular resolution of the HST images is degraded to better match the $\sim 1''$ resolution of the MUSE data. This is done by convolving with a Gaussian kernel.

³ <http://ssb.stsci.edu/pysynphot/docs/>

⁴ <http://www.stsci.edu/hst/observatory/crds>

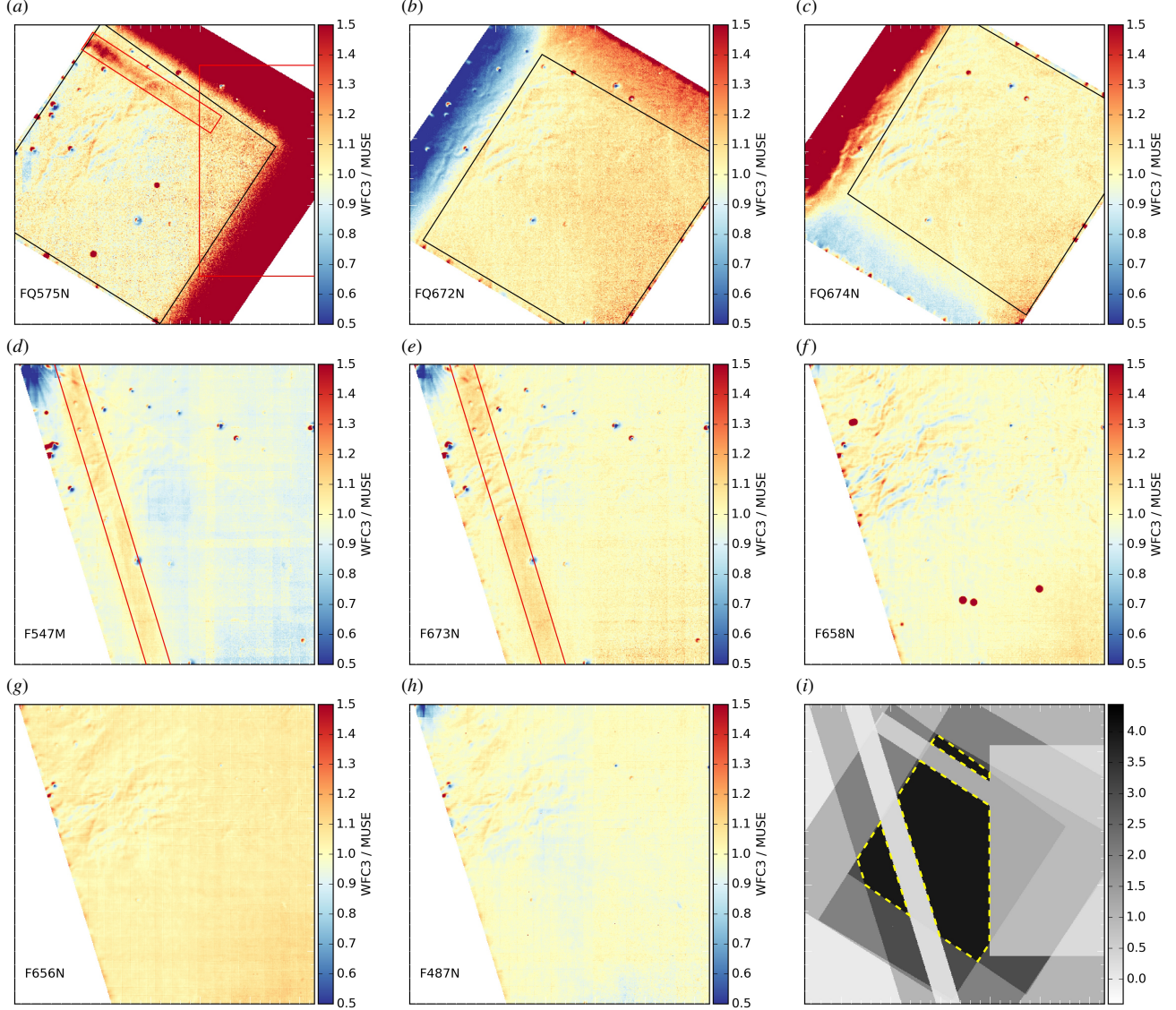


FIG. 11.— Ratios of WFC3 filter images to synthetic filter images derived from the MUSE spectral cube. Each box shows a $90'' \times 90''$ field centered on the Orion S region. The top row of panels shows the quad filters: (a) FQ575N, (b) FQ672N, (c) FQ674N. Hollow black boxes outline the nominal usable portion of the data for each quad filter, which in each case is roughly 1/6 of the full WFC3 chip. Red hollow boxes in (a) outline problematic regions of the FQ575N image, as discussed in the text. Panel (d) shows the medium-band continuum filter F547M, while the following four panels show the regular narrow band filters: (e) F673N, (f) F658N, (g) F656N, (h) F487N. The last panel, (i) shows the superposition of all the usable areas (dark) and unusable areas (light) of the different filters. The combined usable area (in three contiguous portions) is shown outlined by yellow dashed lines.

W2. The HST images are then resampled to the same $0.2''$ pixel scale as the MUSE synthetic filter images. This is carried out via the MOPEX projection algorithm (Makovoz & Khan 2005), as implemented by the `mProjectPP` module of the Montage toolkit.⁵

The resulting images can now be directly compared. In Figure 11 the ratio of the WFC3 to synthetic MUSE images is shown. If there were no systematic errors in either of the WFC3 or MUSE datasets, then this ratio would be constant, apart from variations due to noise. If, in addition, the filter throughput profiles in the CRDS database were perfectly accurate, then each ratio would be unity, corresponding to light yellow in the divergent color scheme used in the figure. Red colors correspond to ratios larger than unity, while blue colors correspond to ratios smaller than unity.

Small-scale deviations in the ratio are mainly due to imperfect astrometric alignment of the two datasets. We find that the MUSE cube has wavelength-dependent astrometric distortions at the level of a fraction of the $0.2''$ pixel size, which we have not attempted to correct. As a result, the alignment is better in the south of the field than in the north, and better at longer wavelengths. Due to the optical design of the camera, the quad filters (top row of panels) have unusable strips along two edges of the displayed field, with the usable portion outlined by the black quadrilateral in the figure.

Stray light in the WFC3 camera, due to the proximity of the bright Trapezium stars located just off the top-left corner of the displayed field, is an issue for those filters that admit a significant portion of continuum radiation. This is the case for FQ575N

⁵ <http://montage.ipac.caltech.edu>

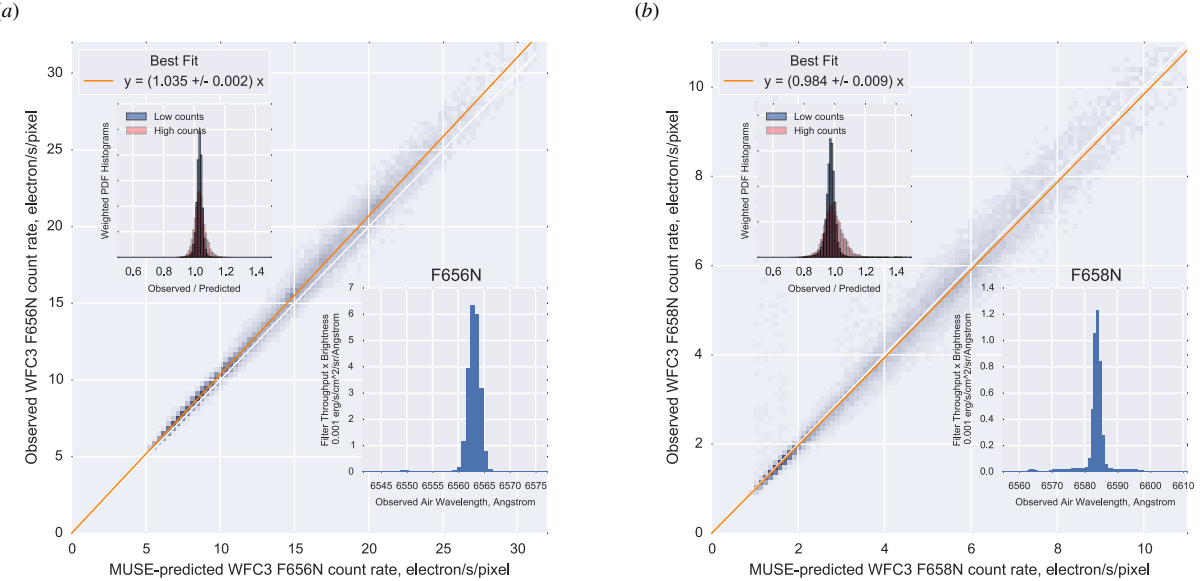


Fig. 12.— Results of spectrophotometric calibration of the WFC3 filters: (a) F656N and (b) F658N. The vertical axis of the principal plot is the observed WFC3 filter count rate after resampling at the 0.2'' pixel size of the MUSE spectrophotometric observations. The horizontal axis of the principal plot is the predicted count rate calculated by folding the MUSE spectrum through the nominal WFC3 filter throughput profile. The grayscale intensity represents the two-dimensional histogram over the entire usable WFC3 field of these two quantities, weighted by the count rate of each pixel. The red line is the optimum linear fit to the relationship. The lower right inset plot shows the product of the MUSE spectrum (integrated over the entire field) and the filter throughput profile. The upper left inset plot shows the distribution of deviations from the linear fit for two subsamples of pixels: the red histogram shows the subsample with larger than average line/continuum ratio, while the blue histogram shows the subsample with smaller than average line/continuum ratio.

(Fig. 11 panel *a*), F547M (panel *d*), and F673N (panel *e*), where the contaminated regions are shown outlined by long thin red boxes. Remaining spatial variations in the ratio will be due to systematic photometric calibration errors in one or other of the datasets. Flat fielding problems are investigated by fitting a bilinear function to the ratio images. For most of the filters, the linear gradient corresponds to changes at the 2 to 5% level across the field, but for FQ672N a stronger gradient of 15% is found. This can be clearly seen in Figure 11(*b*), where the useable portion (black quadrilateral) of the image smoothly transitions from predominantly yellow pixels at the upper left to predominantly red pixels at the lower right. The position angle of the gradient is closely aligned to the pixel axes of the WFC3 chip, which leads us to believe that it is the WFC3 data that is at fault here. We correct for these linear gradients in all subsequent processing.

Another problematic region is the right corner of the FQ575N filter, shown in Figure 11(*a*). The area outlined by the large red rectangle has anomalously high values of the WFC3/MUSE ratio, but in this case it is difficult to say which of WFC3 or MUSE is at fault. The excess is more than 10% and given how critical this filter is to T determinations we discard this portion of the data as a precaution. The final usable region of the WFC3 data is given by the intersection of the usable portions of each filter, and is shown outlined with yellow dashed lines in Figure 11(*i*).

We are finally in a position to determine the absolute values of the ratios, which will provide a check on the calibration of the WFC3 filter transmission amplitudes. In Figures 12 to we show the joint distributions of the WFC3 and synthetic MUSE count rates for only those pixels lying within the usable region outlined in Figure 11(*i*). The orange line shows the best-fit ratio, which can be used to correct the T_λ^j throughput values. The lower-right inset box in each figure shows the product $I_\lambda T_\lambda^j$, which goes into the integral of equation (B1).

All of the fits shown in these figures are forced to pass through the origin, which is equivalent to supposing that there are no errors in the zero points of either the WFC3 or the MUSE data. In order to test this hypothesis, we divide the pixels into a faint and a bright subset, each containing half of the total flux. We show in the upper left panel of each figure separate histograms of the ratio WFC3/MUSE for the two subsets. For nearly all of the filters, the histograms are very similar between the two subsets (strong overlap between the red and blue histograms in the inset plots), but this is not the case for the broadest filter F547M, shown in Figure 14(*a*), for which the ratio in the fainter subset is significantly smaller than that in the brighter subset.

One possible origin of this discrepancy could be a small error in the bias level of the MUSE cube. In order to bring the faint and bright subset ratios into agreement, one requires a shift in the bias level of 20 in units of $10^{-20} \text{ erg s}^{-1} \text{ cm}^{-2} \text{ \AA}^{-1}$, which is roughly 7% of the continuum brightness in the very faintest observed region (the Dark Bay extinction feature). The effect of this shift is illustrated in Figure 16, where it can be seen to dramatically improve the consistency of the fit to the F547M filter, giving a mean ratio very close to unity for both the faint and bright subset. However, as can be seen in panel (*b*) of the figure, the same shift worsens the fit to the FQ575N filter. This is to be expected because the fit to FQ575N was already good without this “correction”, and both filters are dominated by continuum emission (at least for the fainter regions) so that the larger number of MUSE wavelength pixels that contribute to the F547M bandpass is almost exactly compensated by the higher count rate. The same is true for the F673N filter, which also sees a worsening of the quality of fit due to this shift. It is therefore hard to justify making this adjustment to the MUSE bias level.

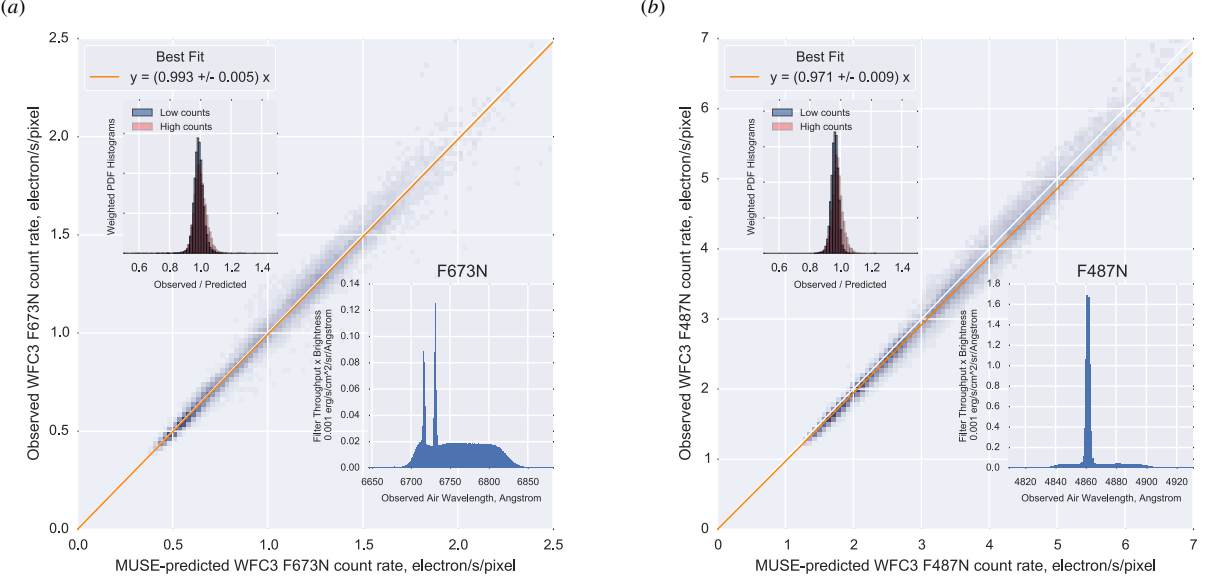


FIG. 13.— Same as Fig. 12 but for (a) F673N and (b) F487N

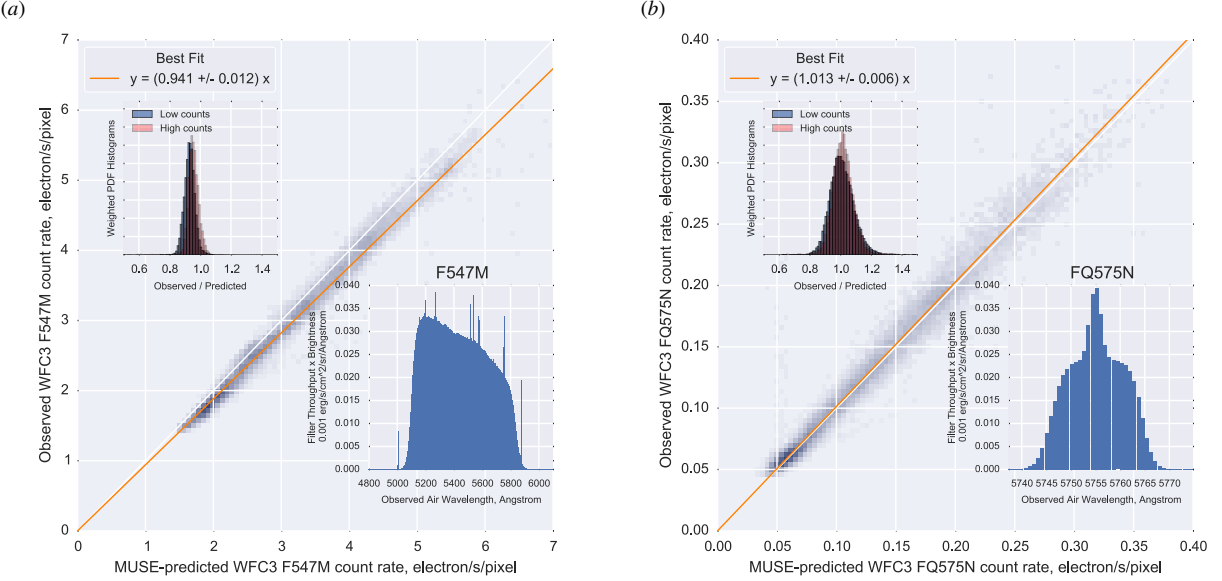


FIG. 14.— Same as Fig. 12 but for (a) F547M and (b) FQ575N

Of course, exactly the same improvement in the F547M fit quality could be obtained by shifting the zero point of y axis, instead of the x axis. This would correspond to a calibration error in the bias level or dark current of the WFC3 image, which in principle might apply to a single filter (unlike similar errors in the MUSE data, which must affect all filters in the same wavelength range). The required shift is of order $0.1e^- s^{-1} pixel^{-1}$, or about $70e^- pixel^{-1}$ over the full exposure time. For comparison, the median dark current for the epoch of our observations is less than $0.002e^- s^{-1} pixel^{-1}$, so it is impossible that any inaccuracy in the dark current subtraction could cause such a large offset. We have manually inspected the overscan regions of the raw images and do not find any evidence of problems in the bias subtraction. It is also worth noting that the quad filters have count rates 30 times lower than F547M, but exposure times that are only 3 times longer, so that even a 10 times smaller zero-point shift than this would be sufficient to upset their calibration. We therefore conclude that there is insufficient motivation to adopt such a large shift for the F547M filter, however tempting it may be to force the calibration ratio to be unity.

B.2. Comparison of spectrally derived and filter-derived line ratios

Given a satisfactory calibration of the WFC3 filter throughputs, as in the previous section B.1. It still remains to demonstrate that the matrix inversion method outlined in Appendix A can deliver accurate line ratio measurements. In order to cleanly isolate the effects of filter-based continuum subtraction we first make the comparison purely *within* the MUSE dataset, by comparing line ratios derived from the synthetic filter images prepared as in steps M1 to M3 above, with those derived directly from the MUSE

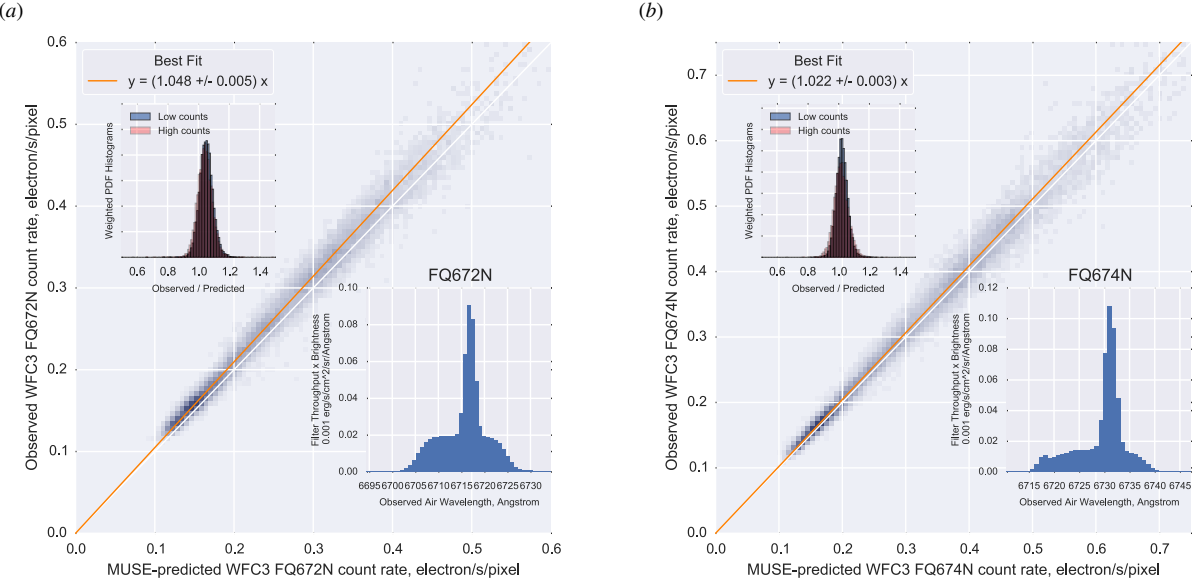


FIG. 15.— Same as Fig. 12 but for (a) FQ672N and (b) FQ674N

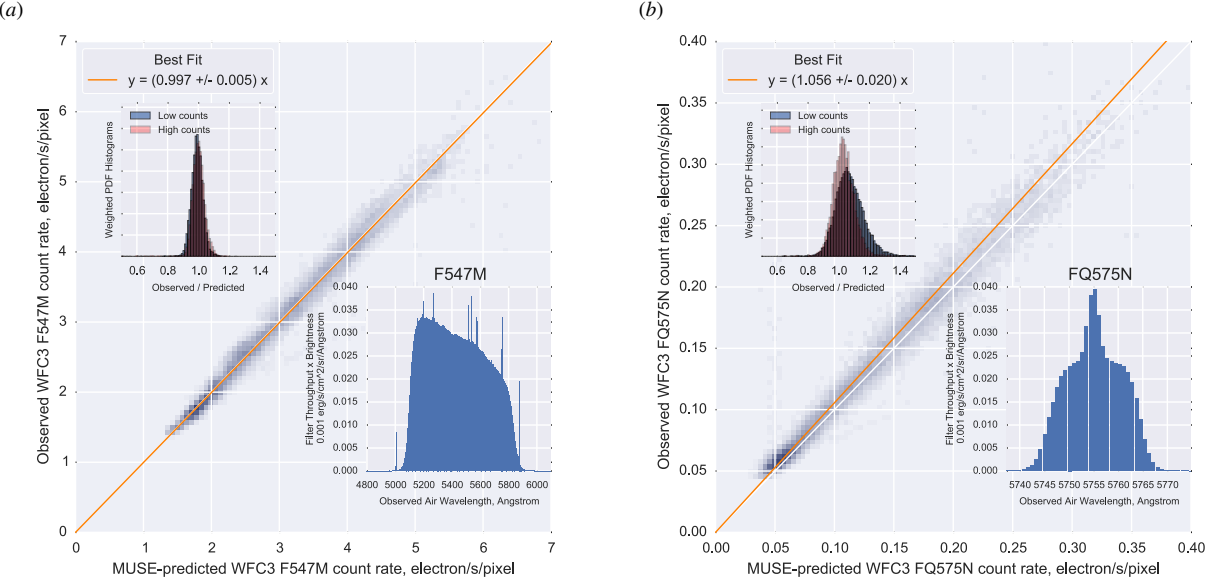


FIG. 16.— Same as Fig. 14 but after subtracting a small constant value per voxel from the fluxes in the MUSE cube. This improves the consistency of the fit to the F547M ratios (panel a) but worsens the consistency of the fit to the FQ575N ratios (panel b), and also the F673N ratios (not illustrated).

data. For the latter, we extracted line fluxes via the following steps:

- L1. Three wavelength windows are defined with respect to the rest wavelength of each line: an inner window spanning the range $\Delta\lambda = [-4, +4]$ Å and two outer windows spanning the ranges $\Delta\lambda = [-8, -4]$ Å and $\Delta\lambda = [+4, +8]$ Å.
- L2. A mean continuum level is found by averaging the flux in the two outer windows, which is subtracted from the profile in the inner window. For cases where a non-target line is present in one of the outer windows, only the uncontaminated window is used, but this is not the case for any of the target lines of this study. Although the C II 6578 line is at $\Delta\lambda = -5.4$ Å with respect to [N II] 6583, it is too weak to significantly affect the continuum estimate.
- L3. The first 3 velocity moments of the line profile are calculated by integrating over the inner window. In the present study, only the total line flux is used.

We then used Equation (A11) in three successive approximations, shown in the top to bottom rows of Figure 17:

- R1. Setting to zero all the filter correction coefficients α , β , and γ so that $I_1/I_2 = (\lambda_2 T_2^{\text{II}} R_1)/(\lambda_1 T_1^{\text{I}} R_{\text{II}})$, which is equivalent to assuming that there is no continuum emission in the narrow-band filters.

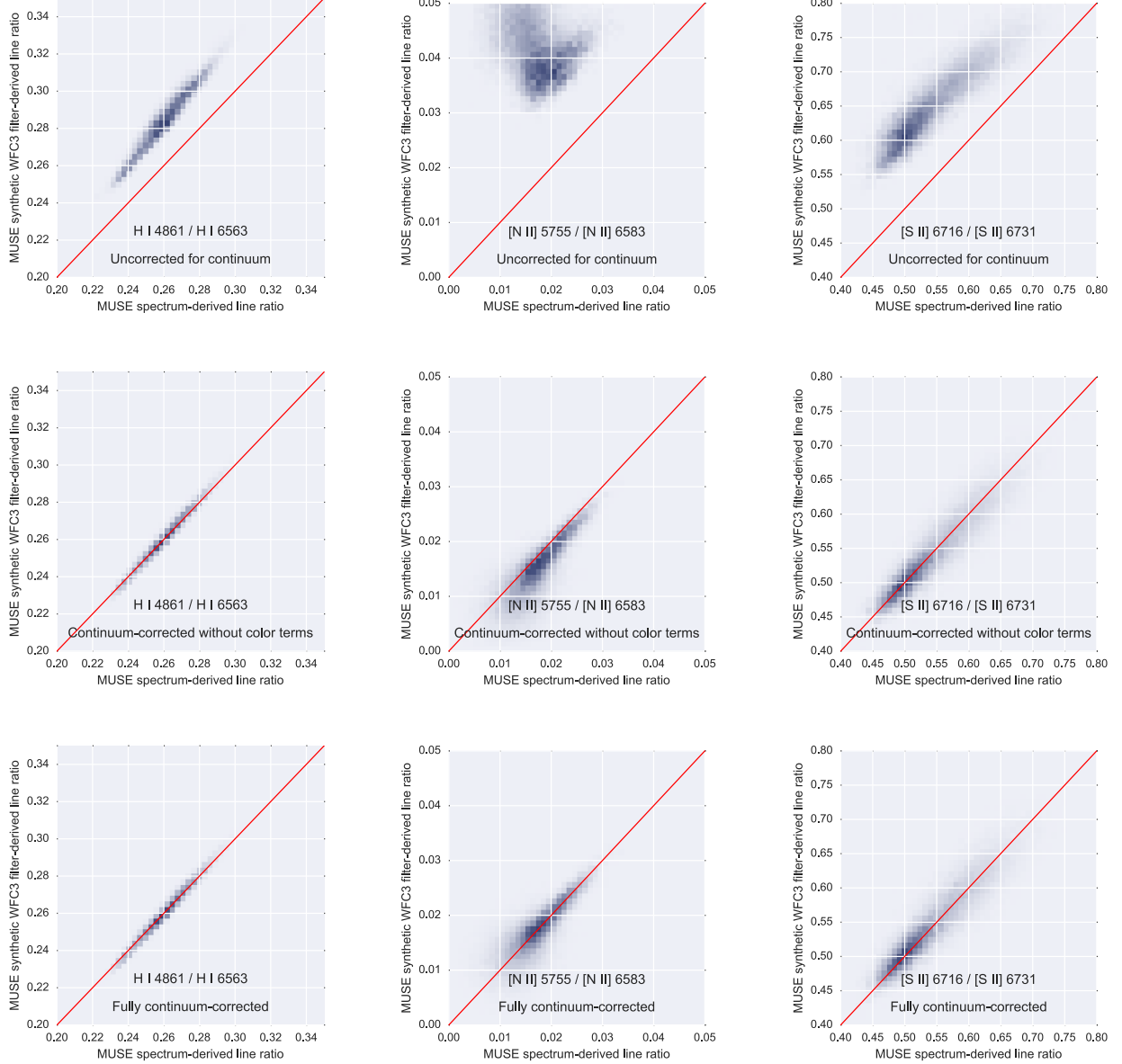


FIG. 17.— Successive improvements in line ratio estimation using synthetic filters with the MUSE dataset, shown on the y axis. In each case, the x axis is the “correct” line ratio as calculated directly from the spectrum. The top row is for a naive estimation of the line ratio from the narrow band filters alone. The middle row includes the broader band filter to correct for the continuum, but assumes that the continuum spectrum is flat. The bottom row is the same, but accounting for an average continuum slope.

- R2. Using the filter correction coefficients, but setting the color terms $\tilde{k}_{I,III} = \tilde{k}_{II,III} = 1$, which is equivalent to assuming no non-target line contamination of the wide-band filter and that the continuum spectrum is flat between the wide-band and narrow-band filters.
- R3. As previous, but setting each color terms to an average value determined from the spectrum of the entire nebula, as shown in Figure 18.

From the top row of Figure 17 it can be seen that all three of the diagnostic ratios are severely affected by continuum contamination of the narrow-band filters, even for the relatively high equivalent width hydrogen Balmer lines. The middle row shows that assuming a flat continuum is sufficient for correcting the Balmer decrement 4861/6563 and [S II] 6716/6731 ratios, but that the filter-derived [N II] 5755/6583 ratio still shows systematic errors. These errors are adequately corrected by accounting for the continuum color, as seen in the bottom row.

So far, have separately tested the two parts of the chain by which line ratios are derived from imaging through narrow band filters. We now put these two parts together and directly compare the line ratios obtained from MUSE spectra and WFC3 imaging.

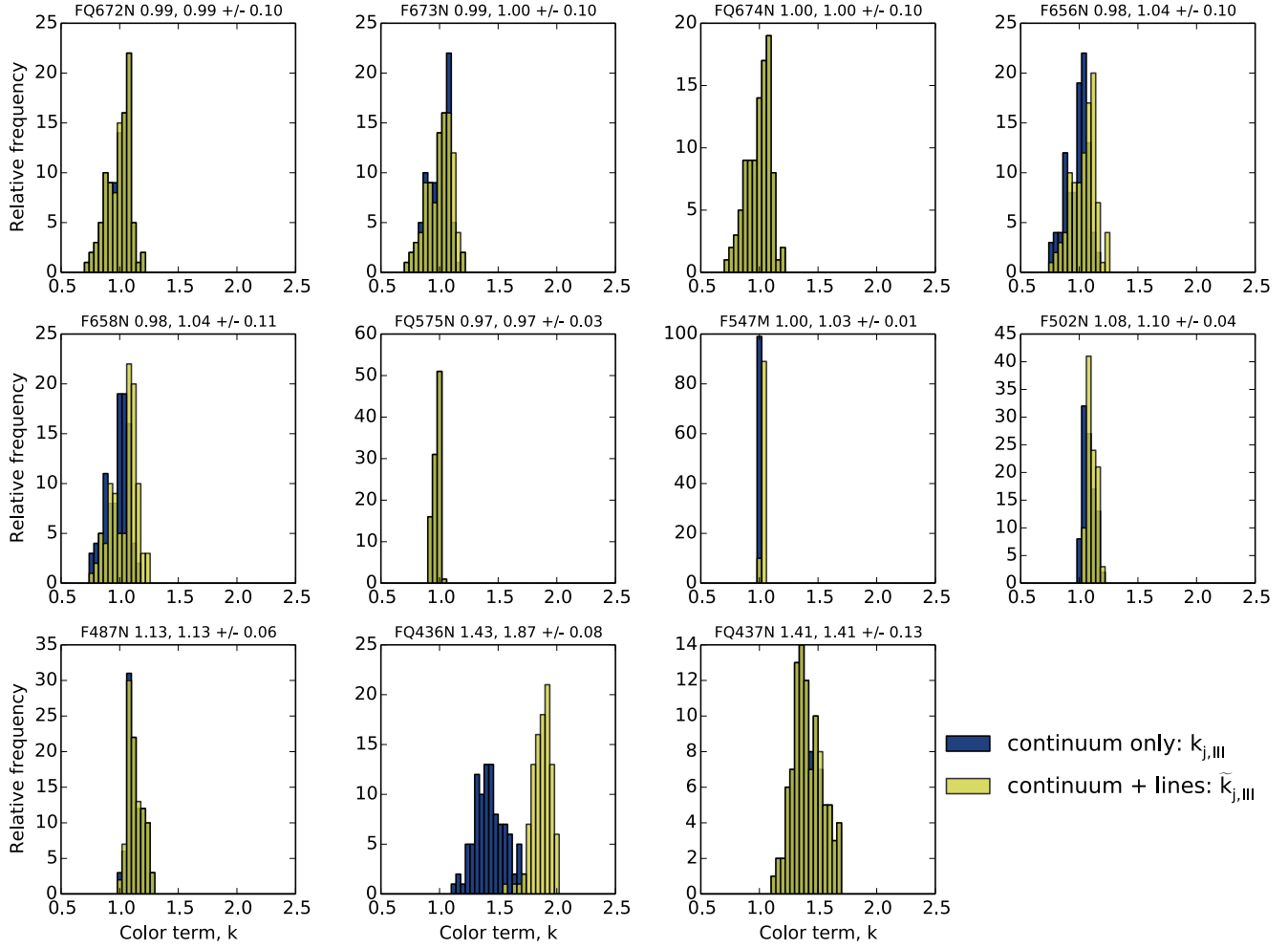


FIG. 18.—Observationally determined histograms of the color correction terms, k , for each filter with respect to the F547M filter, measured from spectrophotometry of the Orion Nebula (O'Dell & Harris 2010). The blue histograms show the ratio of the mean continuum intensity in each filter to that in F547M, as given by equation (A8), while the yellow histograms include the additional effect of non-target emission lines and correspond to the numerator (for filters I and II) or denominator (for filter III) of the fraction on the RHS of equation (A9).

B.3. Sensitivity of derived line ratios to calibration errors and plane-of-sky spectral variations

The finite accuracy with which the MUSE calibration determines the integrated WFC3 filter throughputs leads to a systematic uncertainty in any line ratios derived from those filters. The sensitivity to such effects of the key temperature sensitive [N II] ratio and density sensitive [S II] ratio are shown in Figure 20.

Note that it is only the amplitude T_m^j of the filter transmission that is allowed to vary here. The filter width and central wavelength are assumed to be fixed at the values determined by pre-launch measurements.

Two further unwanted sources of variation in derived line ratios arise from point-to-point variations in the spectral shape of the nebular continuum and in the Doppler shifts of the target emission lines. The first of these enters via the color terms k , (Eqs. (A8, A9)) that describe the relative change in the continuum strength between the broad filter and the narrow filters. The optical continuum in the Orion Nebula is a combination of starlight scattered from dust, together with radiative recombination emission (principally the Paschen continuum of hydrogen) and two-photon emission. The Paschen continuum rises to the red, whereas both scattered starlight and two-photon continuum rise to the blue. The changing relative contributions of these different mechanisms across the face of the nebula

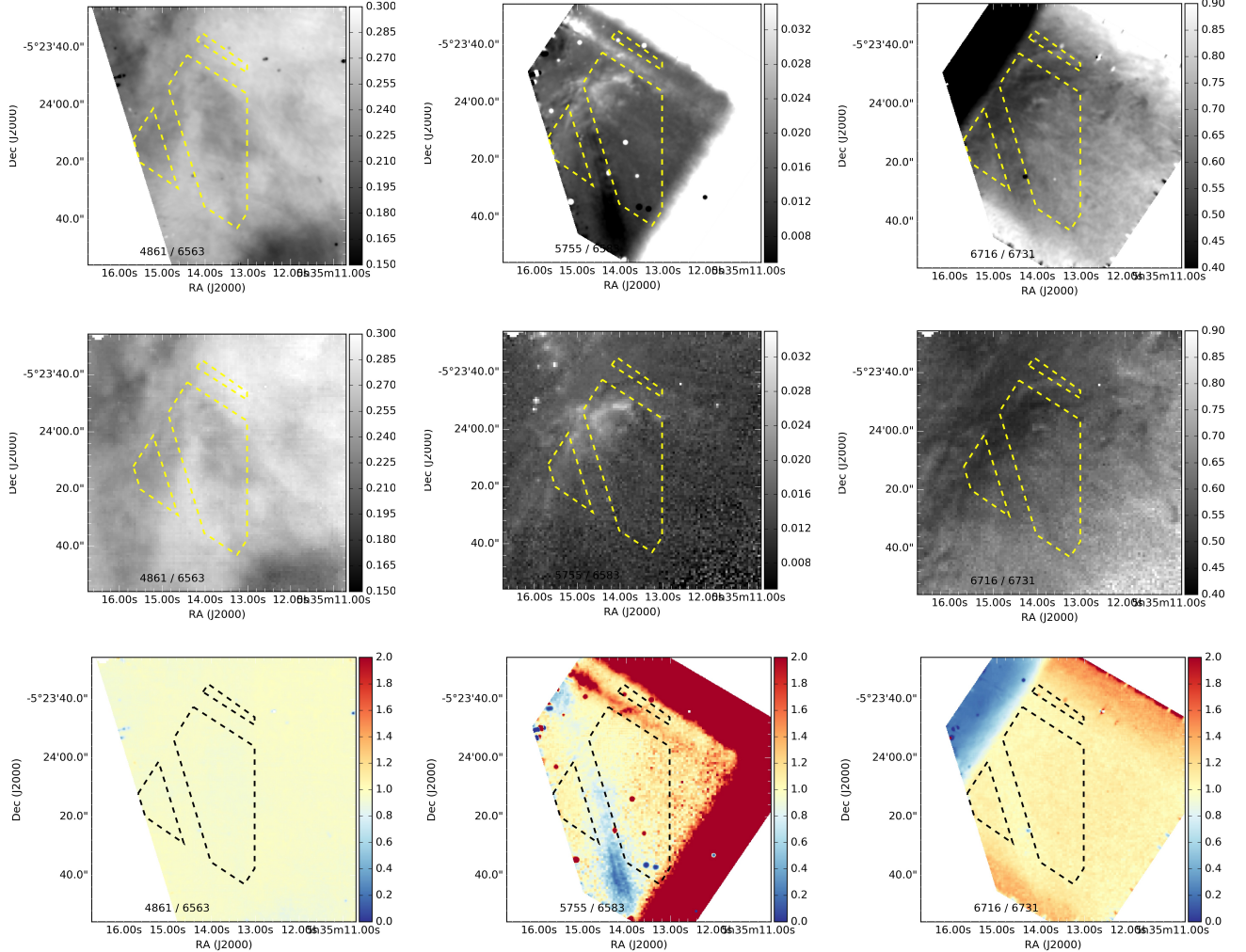


FIG. 19.— Comparison of emission line ratios derived from WFC3 filter images (top row) and MUSE spectra (middle row). The WFC3 images have been smoothed and resampled at the MUSE resolution as described in B.1. The bottom row shows the ratio between these two methods of determining the line ratios, which should be unity if both methods are perfectly calibrated.

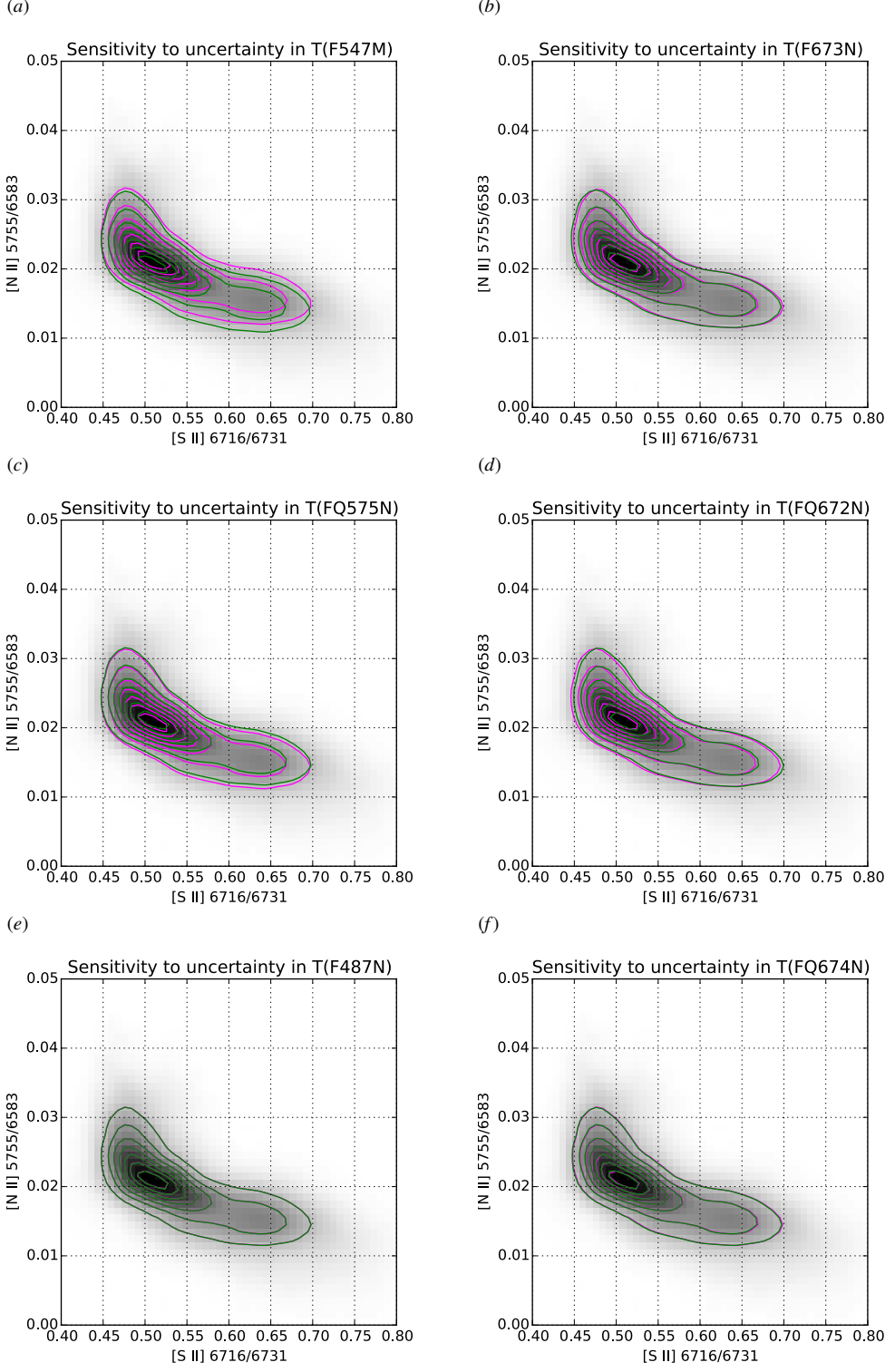


FIG. 20.—Sensitivity of filter-derived $[S\text{ II}]$ and $[N\text{ II}]$ line ratios to systematic uncertainties in the filter peak transmissions. Magenta and green contours show the results of varying T_m^j by ± 1 standard deviation, respectively, about the best fit values determined in § B. (a) F547M, used to measure the continuum for the $[N\text{ II}]$ lines; (b) F673N, used to measure the continuum for the $[S\text{ II}]$ lines; (c) FQ575N, which targets the weak $[N\text{ II}]$ auroral line; (d) FQ672N, which targets the shorter wavelength component of the $[S\text{ II}]$ doublet; (e) F487N, used to estimate the foreground reddening; (f) FQ674N, which targets the longer wavelength component of the $[S\text{ II}]$ doublet.

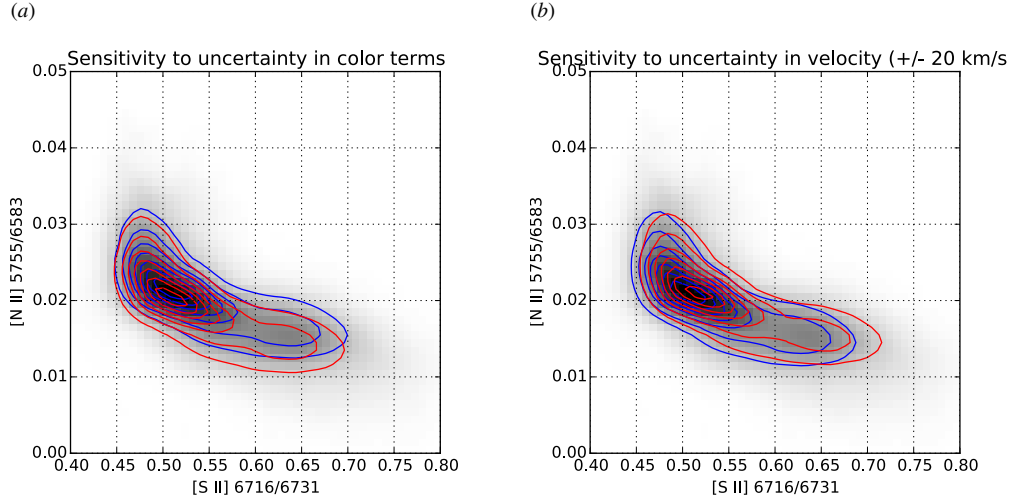


FIG. 21.— Sensitivity of filter-derived $[\text{S II}]$ and $[\text{N II}]$ line ratios to spatial variations across the nebula of the color of the continuum and (b) the Doppler shift of the emission lines.